

Inspiring Black-Hole Binary Spacetimes: Transitioning from Analytical to Numerical Techniques

Yosef Zlochower,¹ Hiroyuki Nakano,² Bruno C. Mundim,³ Manuela Campanelli,¹ Scott Noble,⁴ and Miguel Zilhão⁵

¹*Center for Computational Relativity and Gravitation,
Rochester Institute of Technology, Rochester, NY 14623, USA*

²*Department of Physics, Kyoto University, Kyoto 606-8502, Japan*

³*Institut für Theoretische Physik, Johann Wolfgang Goethe-Universität,
Max-von-Laue-Str. 1, 60438 Frankfurt am Main, Germany*

⁴*Department of Physics and Engineering Physics, The University of Tulsa, Tulsa, OK 74104*

⁵*Departament de Física Fonamental & Institut de Ciències del Cosmos,
Universitat de Barcelona, Martí i Franquès 1, E-08028 Barcelona, Spain*

Here we explore how a recently developed analytical black-hole binary spacetime can be extended using numerical simulations to include the merger proper. The analytic spacetime solves the Einstein field equations approximately, with the approximation error becoming progressively smaller the more separated the binary. Importantly, the analytic spacetime encodes the past history of the binary in the radiation zone and the tidal fields distorting each black hole. To continue the spacetime through merger, we need to smoothly transition from the analytical spacetime to a numerically derived spacetime. We do this by using the analytical spacetime for an equal-mass, nonspinning black hole binary as initial data for a subsequent numerical evolution of the metric, and experiment with how this transition can be accomplished. We test our procedure for an equal-mass binary at a separation of $D = 20M$, and evolve for six orbits. We find that small constraint violations can have large dynamical effects, but these can be removed by using a constraint damping system like the conformal covariant formulation of the Z4 system. We find agreement between the subsequent numerical spacetime and the predictions of post-Newtonian theory for the waveform and inspiral rate that is within the post-Newtonian truncation error.

PACS numbers: 04.25.dg, 04.30.Db, 04.25.Nx, 04.70.Bw

I. INTRODUCTION

The field of numerical relativity (NR) has progressed at a remarkable rate since the breakthroughs of 2005 [1–3], when it first became possible to simulate the late-inspiral, plunge, merger, and ringdown of black-hole binaries (BHBs). Recently, Szilagyi et al. [4] were able to perform a fully nonlinear NR simulation of an inspiraling binary for 350 orbits. This is a remarkable achievement, but the scaling of the inspiral time with the initial separation $T \sim D^4$ means that evolving a binary through the long inspiral is prohibitively expensive, even for highly efficient codes. Such a simulation becomes even more expensive when one is interested in performing long-term dynamical evolutions of relativistic magnetohydrodynamics (MHD) circumbinary disks around inspiraling supermassive BHBs (SMBHBs). This is because the circumbinary gas can exhibit significant secular variations on the time scale of hundreds to thousands of binary orbits.

In order to make these long-term simulations possible, our group developed a complementary approach to treat dynamical BHB spacetimes. In a series of papers [5–9] we used an analytic spacetime that is an approximate solution to the Einstein field equations in the inspiral regime to describe the evolution of the accretion disks surrounding the binary and each of the individual BHs.

Our initial approach [5], was one in which relativistic effects were present but relatively small. In the situation

when gravity is weak [$r_g/r = GM/(rc^2) \ll 1$] and motions are slow [$(v/c)^2 \ll 1$], the post-Newtonian (PN) approximation gives a very good description of spacetime. One can then simply construct a PN metric which takes energy loss from the binary into account, accurately modeling both the mass loss and inspiral of the binary [10]. Using a spacetime accurate to 2.5PN order (i.e., including terms up to $\sim (r_g/r)^{5/2}$), but describing the binary orbital evolution to 3.5PN, we demonstrated that circumbinary disks can track the inspiral of a SMBHB until the binary practically reaches the relativistic merger regime [5]. The shortcoming of this approach was that the PN metric was not valid very close to the BHs, and consequently, we excised any material that fell within 1.5 binary separations. This prevented us from studying the dynamics of the gas all the way down through the horizons of each BH.

In a more recent paper [7], we extended the metric to cover the full BHB spacetime up to the rapid plunge state. We did this by extending the framework established in Refs. [11–13] for constructing a spacetime metric valid for initial data, i.e., a metric accurate for all spatial points but in a very small time interval, to develop a metric valid for arbitrary times. In this approach, the *near zone* (NZ), i.e., a zone well outside the two BHs, but less than a gravitational wavelength from the binary, is still described using a PN expansion. In the *far zone* (FZ), i.e., farther than one wavelength from the binary, the metric is described by a PN expansion. Finally, near

each BH, i.e., in the *inner zone* (IZ), the metric is described using a perturbed Kerr (here Schwarzschild) BH. The metrics covering the different zones are smoothly stitched together using asymptotic expansions and transition functions in their overlapping regions of validity.

This approach allows us to follow inspiraling SMBHBs over hundreds to thousands of binary orbits, the timescale on which gas accumulates, without having to solve the Einstein's equations numerically. Therefore the advantages are both in terms of computational efficiency and accuracy. Because numerical phase errors tend to increase faster than linearly, these can quickly become larger than the analytic approximation errors at large separations. At close separations, on the other hand, the analytic error dominates.

Here, we explore the possibility of using a hybrid approach, i.e., use the analytic metric for the long inspiral down to separations where our global spacetime metric is still valid, and then transition to a full numerical simulation using the analytic spacetime as initial data. The way to do this is to convert our approximate spacetime prescription into suitable initial data for $3 + 1$ NR evolutions, evolve the data forward in time, and compare both orbital evolution and gravitational radiation output with our approximate solution. The use of PN techniques to generate initial data for BHBs was first developed in Refs. [13–16].

When using the global analytic metric as initial data, the resulting initial data are essentially equivalent (there is only a small difference in the NZ/FZ transition function and the two metric prescriptions coincide at $t = 0$) to the initial data proposed in Johnson-McDaniel et al. [13], and first evolved in Reifenberger and Tichy [17]. Reifenberger and Tichy compared evolutions of Bowen-York data [18] to several different analytic initial data constructions, including Johnson-McDaniel et al.. Our work here extends upon the work of Reifenberger and Tichy by evolving binaries with larger separations (well in the PN regime), and by finding techniques to ameliorate the inaccuracies associated with evolving these data discovered by Reifenberger and Tichy. These inaccuracies arise from both constraint violations, due to the fact that our global metric solves the Einstein's field equations only approximately, and inaccuracy in the PN orbital angular momentum and inspiral rate, which can lead to eccentricity in the numerical binary evolution.

For the current work, we start the full numerical simulations when the binary is separated by $D = 20M$. As shown in Ref. [19], where the authors there explored numerical simulations of Bowen-York data at separations ranging from $D = 100M$ to $D = 20M$, there is good agreement between the predictions of PN theory and numerical simulations at $D = 20M$. Additionally, simulations starting at $D = 20M$ down to merger are possible with our current codes, as demonstrated in Ref. [20].

This paper is organized as follows. In Sec. II, we review how the analytic BHB inspiral metric is constructed, as well as how it is used to generate $3 + 1$ initial data. In

Sec. III, we describe the techniques we used to numerically evolve the spacetime metric. In Sec. IV, we provide details on how the simulations were performed and the key outcomes of these simulations. In Sec. V, we compare the results from the numerical simulation at separations $\sim 20M$ with the predictions of PN theory. Finally, in Sec. VI we discuss our results both in terms of the accuracy of the binary dynamics (e.g., inspiral rate and orbital frequency) and in terms of gravitational waveform generation.

Throughout this paper, we use the geometric unit system, where $G = c = 1$, with the useful conversion factor $1M_{\odot} = 1.477 \text{ km} = 4.926 \times 10^{-6} \text{ s}$.

II. INITIAL DATA

In this paper, we restrict our analysis to non-spinning BHs in quasi-circular orbits. In this context, it is useful to provide a brief review here of our approximate solution to the Einstein's field equations of a BHB spacetime in the inspiral regime [7]. The inclusion of spins, both aligned [6] and unaligned in this spacetime framework will be the subject of future studies.

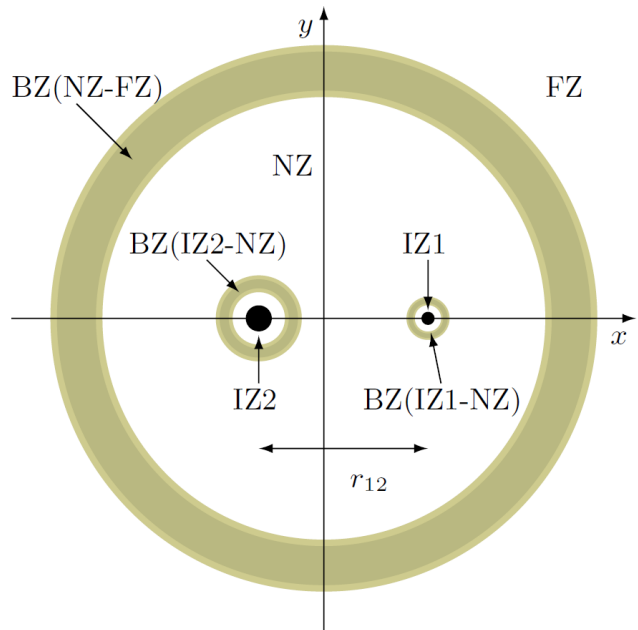


FIG. 1. Schematic diagram of the zones. BH1 and BH2 are denoted by solid black dots, where the orbital separation is r_{12} . The BZs are denoted with gray shells, the outer one representing the FZ/NZ BZ and the two inner ones representing the NZ/IZ BZs (see also Table I). The IZ, NZ and FZ are also shown in the figure.

This framework was first introduced in Refs. [11–13] as initial data for BHB evolutions, and was generalized in Ref. [7] to be a full BHB spacetime. In this framework,

TABLE I. Location of the inner, near, and far zones, as well as the buffer zones joining them. Here r_{in} and r_{out} are the approximate inner and outer boundaries of a given zone, m_i is the mass of BH i , r_i is the coordinate distance to BH i , r_{12} is the binary separation, and λ is the wavelength of gravitational radiation emitted by the binary.

Zone	r_{in}	r_{out}	Region
IZ BH1 (r_1)	0	$\ll r_{12}$.
IZ BH2 (r_2)	0	$\ll r_{12}$.
NZ (r_A)	$\gg m_A$	$\ll \lambda$.
FZ (r)	$\gg r_{12}$	∞	.
IZ-NZ BZ	.	.	$m_A \ll r_A \ll r_{12}$
NZ-FZ BZ	.	.	$r_{12} \ll r \ll \lambda$

the spacetime is constructed by asymptotically matching metrics in three different zones characterizing three different spacetime regions of validity for different analytic metrics: (i) a far zone (FZ) where the spacetime can be described by a two-body perturbed flat spacetime with outgoing gravitational radiation and where retardation effects are fully accounted for; (ii) a near zone (NZ) which is less than one GW length from the center of mass of the binary (but not too close to each BH) that is described by a PN metric (this includes retardation effects at a perturbative level and binding interactions between the two BHs); and (iii) inner zones (IZs) that are described by perturbed Schwarzschild (or Kerr) BHs. The full spacetime is then constructed by smoothly transitioning from zone to zone in the so-called buffer zones (BZs). A schematic diagram of these zones, and a table describing where the zone boundaries are located are provided in Fig. 1 and Table I (these figure and table were also presented in Refs. [6, 7]).

III. TECHNIQUES

We evolved the BHB initial data using the LAZEV [21] implementation of the moving puncture approach [2, 3] with the conformal function $W = \sqrt{\chi} = \exp(-2\phi)$ suggested by Ref. [22] and the Z4 evolution system [23–25]. Here we use the conformal covariant Z4 (CCZ4) implementation of Ref. [25]. For the CCZ4 system, we again used the conformal factor W . We used centered eighth-order finite differencing for all spatial derivatives, a fourth-order Runge Kutta time integrator, and both fifth and seventh-order Kreiss-Oliger dissipation [26].

Our code uses the EINSTEINTOOLKIT [27–29] / CACTUS [30] / CARPET [31, 32] infrastructure. The CARPET mesh refinement driver provides a “moving boxes” style of mesh refinement. In this approach, refined grids of fixed size are arranged about the coordinate centers of both holes. The CARPET code then moves these fine grids about the computational domain by following the trajectories of the two BHs.

We use AHFINDERDIRECT [33] to locate apparent horizons. We also use the Antenna code [34] to calcu-

late the Weyl scalar ψ_4 .

We measure the distance between the two BHs using the *simple proper distance* or SPD. The SPD is the proper distance between the two BH horizons along the coordinate line joining the two centers. As such, it is gauge dependent, but still gives reasonable results (see Ref. [19] for more details).

To obtain initial data, we use eighth-order finite-differencing of the analytic global metric to obtain the 4-metric and all its first derivatives at every point on our simulation grid. The finite-differencing of the global metric is constructed so that the truncation error is negligible compared to the subsequent truncation errors in the full numerical simulation (here we used finite-difference step size of 10^{-4} , which is 90 times smaller than our smallest gridsize in any of the numerical simulations discussed below). We then reconstruct the spatial 3-metric γ_{ij} and extrinsic curvature K_{ij} from the global metric data. Note that with the exception of the calculation of the extrinsic curvature, we do not use the global metric’s lapse and shift. In order to evolve these data, we need to remove the singularity at the two BH centers. Unlike in the puncture formalism [35], the singularities here are true curvature singularities. We *stuff* [36–38] the BH interiors in order to remove the singularity. Our procedure is to replace the singular metric well inside the horizons with non-singular (but constraint violating) data through the transformations

$$\gamma_{ij} \rightarrow f(r) \gamma_{ij} \quad i \neq j, \quad (1)$$

$$\gamma_{ii} \rightarrow f(r) \gamma_{ii} + (1 - f(r))\Xi, \quad (2)$$

$$K_{ij} \rightarrow f(r) K_{ij}, \quad (3)$$

where

$$f(r) = \begin{cases} 0 & r < r_{\text{min}} \\ 1 & r > r_{\text{max}} \\ P(r) & r_{\text{min}} \leq r \leq r_{\text{max}} \end{cases}, \quad (4)$$

r is the distance to a BH center, and $P(r)$ is fifth-order polynomial that obeys $P(r_{\text{min}}) = P'(r_{\text{min}}) = P''(r_{\text{min}}) = 0$, $P(r_{\text{max}}) = 1$, $P'(r_{\text{max}}) = P''(r_{\text{max}}) = 0$, and Ξ is a large number. The resulting data are therefore C^2 globally. The parameters r_{min} , r_{max} , and Ξ are chosen such that both transitions occur inside the BHs and so that W varies smoothly with negligible shoulders in the transition region and is small at the centers.

IV. SIMULATIONS

The initial data parameters for our BHB simulations are given in Table II. To evolve these data, we used two different grid structures, denoted G1 and G2. Both G1 and G2 had a coarsest grid spanning $0 \leq x \leq 3200M$, $-3200M \leq y \leq 3200M$, and $0 \leq z \leq 3200M$ (we used π -rotation symmetry and z -reflection symmetry). The refinement levels were centered on the two BHs with half-widths of 1600, 800, 440, 220, 110, 55, 25, 10, 5, 2, 0.65,

TABLE II. Initial data parameters. m_1 and m_2 are the masses of the two BHs, D is the orbital separation, $\delta\Omega_{\text{orb}}$ and $\delta\dot{r}$ are the modifications to the 3.5PN orbital frequency and inspiral required to reduce the eccentricity, Ξ is a scale factor (see text), and r_H is the measured horizon radius.

m_1/M	0.5	m_2/M	0.5
D/M	20.00	$M \delta\Omega_{\text{orb}}$	7.88515×10^{-6}
$\delta\dot{r}$	-1.54103×10^{-4}	r_{min}/M	0.05
r_{max}/M	0.25	Ξ	800
r_H/M	0.484		

and 0.25 for G1, and 1600, 800, 440, 220, 110, 55, 25, 10, 5, 2, and 0.75 for G2. Note that while G2 had fewer levels, it proved to be the more accurate grid configuration. Basically, as we previously observed with highly-spinning initial data [39], for these data, far better accuracy is obtained by using coarser level with half-width 1.5 times as large as the horizon radius than by using a smaller half-width and an interior level. In the figures below we denote the resolution of the coarsest grid by h . Our lowest resolution runs had a coarsest resolution of $h = h_0 = 32M$. We increased the resolution by successive factors of 1.2 for the higher resolution runs.

Our initial explorations of the dynamics of these data were based on the standard BSSN formulation [40–42] in the moving puncture approach. However, as shown in Fig. 2, the mass conservation of the BHs was quite poor for BSSN and substantially better for CCZ4. This lack of mass conservation should lead to unphysical binary dynamics (there is some evidence for this in a short BSSN run shown in Fig. 3). We associate this lack of mass conservation with absorption of *strange matter* (i.e., constraint violating fields) by the system. The errors associated with evolving these data with BSSN were first found by Reifenberger and Tichy [17], where, like we do here, they looked at mass conservation, inspiral time, anomalous eccentricity, and constraint violations.

As shown in Fig. 4, the L2 norms of the constraint violations for CCZ4 and BSSN evolutions behave quite differently. The CCZ4 constraints fall to a much lower level (about a factor of 1000 smaller for the Hamiltonian and a factor of 100 for the momentum) than BSSN. For comparison purposes, we performed equivalent evolutions with standard Bowen-York initial data [18]. Important also is where the constraint violations are located. In Fig. 5, we show the Hamiltonian constraint at $t \sim 200M$ for both CCZ4 and BSSN. The BSSN constraints are still quite large and track the BHs. The CCZ4 constraint violations were mostly radiated away. Because of these results, all of our long-term simulations used CCZ4.

Our motivation for using CCZ4 was based on the observation that constraint violations seem to be triggering excess eccentricity by driving an unphysical change in the horizon mass. CCZ4 both exponentially damps out constraint violation and also propagates them off the grid.

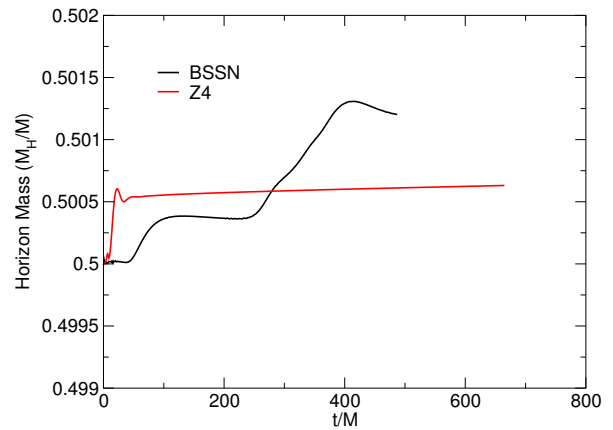


FIG. 2. The individual horizon masses for a BHB with initial separation of 20M for both CCZ4 and BSSN evolutions. The large mass oscillations in the BSSN run are due to absorptions of constraint violations

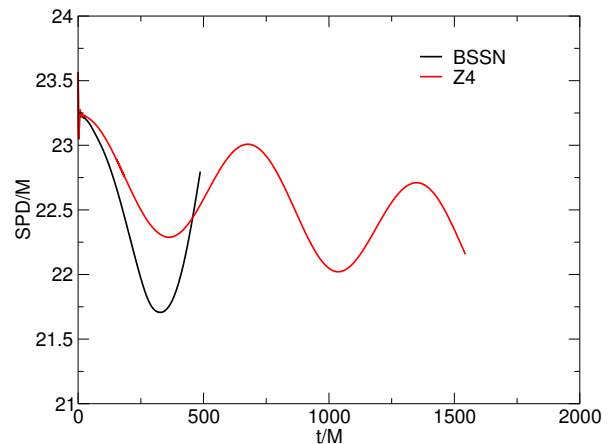


FIG. 3. The SPD versus time for BSSN and CCZ4 simulations of the same initial data. A lack of mass conservation drives the increase in eccentricity seen in BSSN.

As shown in Fig. 6, we see clear convergence of the L2 norm of the momentum constraint violation, while the Hamiltonian constraint violation, while small, seem to bottom out at about 10^{-8} .

The overall efficacy of using CCZ4 to drive the constraint violations to zero can be measured by examining in detail how well the horizon masses are conserved. As show in Figs. 7 and 8, there is a relatively strong linear trend in the mass that, while convergent, is substantially larger than the Bowen-York result. Here we also see a significant advantage to using the G2 grid structure and higher-order dissipation. Note that even with the highest resolution runs, the horizon mass increase is an order of magnitude larger than for Bowen-York data evolved with CCZ4. Since the Bowen-York data were evolved with the same evolution system and grid structure, it appears that there are peculiarities associated with the analytic initial data driving the mass increase. One possibility which we have not explored in detail here is that

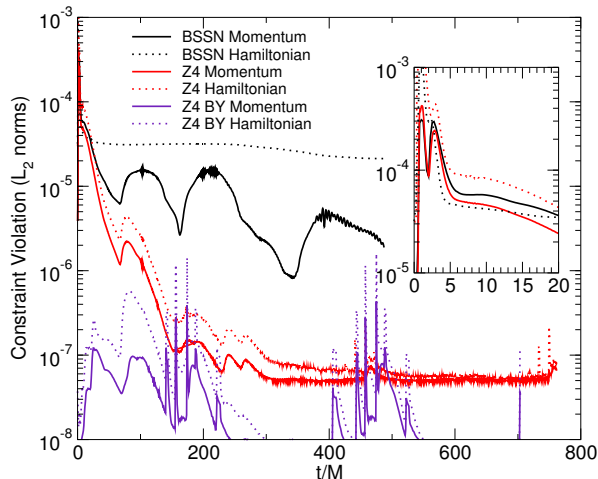


FIG. 4. Time evolution of the L2 norms of the constraint violations for BSSN and CCZ4 evolutions. Note how the BSSN Hamiltonian constraint remains relatively high while the CCZ4 constraints quickly fall to about 10^{-7} . Also shown is the L2 norms of the constraint violations for an evolution of Bowen-York data with CCZ4. The Bowen-York data leads to constraint violations that are on average a factor of 10 below constraint violations for the new data.

the methods used to *stuff* the BHs may be affecting the mass conservation. The other candidate would be residual constraint violations. Even for our highest resolution G2 run, the average constraint violation on the horizon surface at late time was 50% larger than for Bowen-York (the global constraint violations were, on average, an order of magnitude larger, as shown in Fig. 4). As observed in Ref. [8], differences in accuracy of the spacetime at this level will likely not be important for MHD simulations.

V. COMPARISON TO PN

After applying the procedure of Ref. [43] to our data (we found that we needed to set $M\delta\Omega_{\text{orb}} = 7.88515 \times 10^{-6}$ and $\delta\dot{r} = -0.000154103$), we were left with a residual eccentricity of $e = 0.002$, which was small enough for this test. The eccentricity reduction here is complicated by the fact that the amount of constraint violating fields absorbed by the BHs changes as the trajectories are modified. This in turn, leads to a more complicated dependence of the eccentricity on the orbital parameters than is seen for constraint satisfying data. In Fig. 9, we show the SPD versus time and PN separation versus time. Since the SPD at $t = 0$ is larger than $20M$ we translate the SPD vertically. While it is interesting that the numerical SPD matched the PN separation reasonably well, these are not gauge invariant quantities. To have a more gauge invariant measure of the accuracy of the evolution we compare the waveform (as extracted at $1600M$) with the 3.5PN prediction for quasicircular orbits [44] (similar to what was done in Ref. [19] and [45]). When extracting

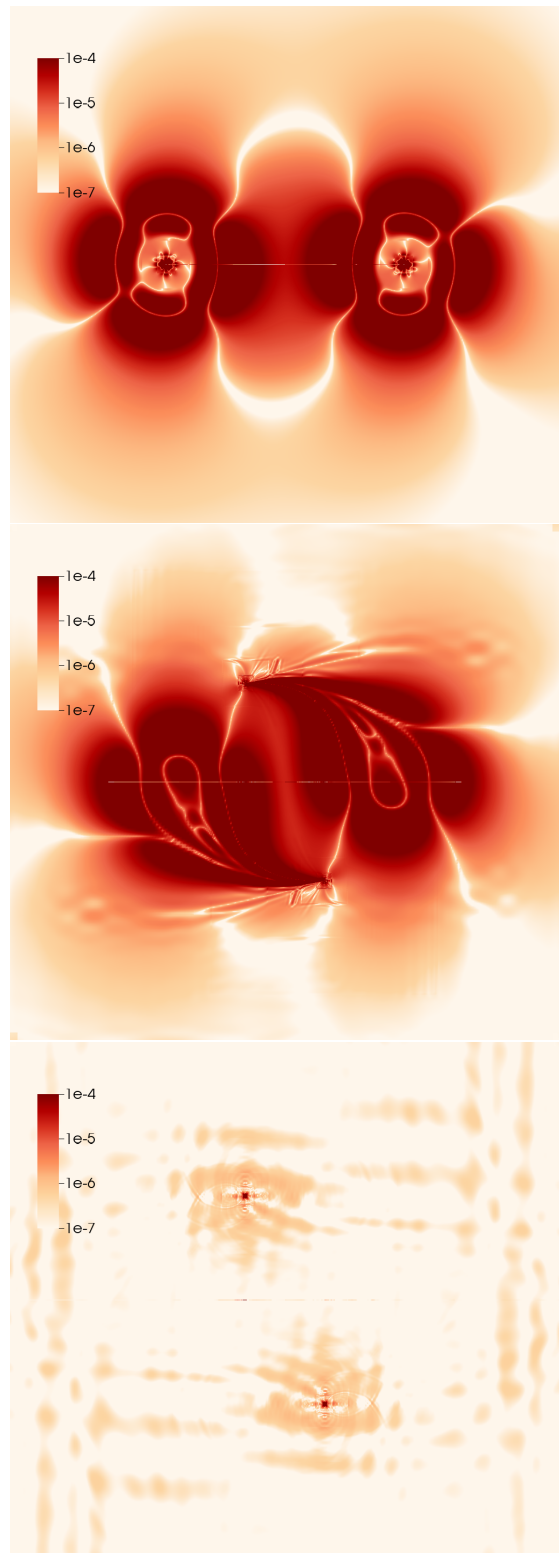


FIG. 5. The Hamiltonian constraint on the xy plane near the two BHs at $t = 0$ (top), $t \sim 200M$ for BSSN (middle), and $t = 200M$ for CCZ4 (bottom) evolutions. The scale is logarithmic and goes from 10^{-7} to 10^{-4} . The constraint violations for the BSSN simulation match closely the violations on the initial slice, while the CCZ4 violations are only large inside the horizons. In each plot the axes range from -25 to 25 in both the x and y directions.

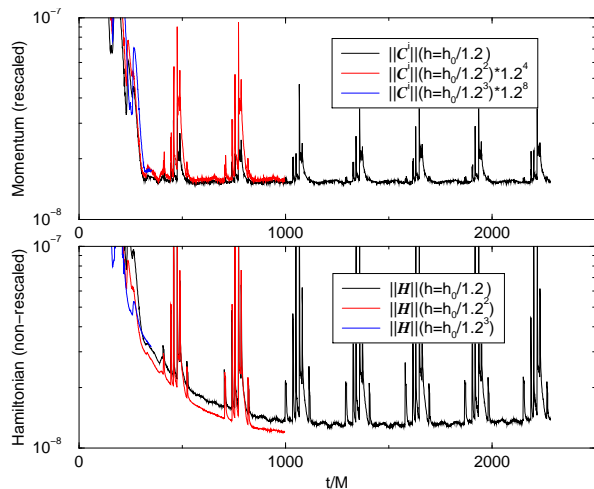


FIG. 6. The L2 norms of the momentum and Hamiltonian constraint violations. The momentum constraints have been rescaled by a factor of $(h_0/h)^4$, where h is the central resolution and h_0 is the central resolution of the coarsest simulation. Note that the Hamiltonian violations have not been rescaled.

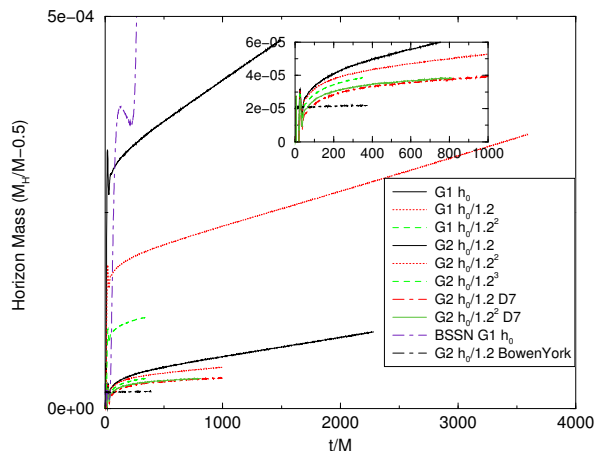


FIG. 7. The mass of the individual horizons versus time for the CCZ4 simulations using the G1 and G2 grid structures, as well as the G2 grid structure and seventh-order dissipation (D7). There are two triplets of black (solid), red (dotted), and green (dashed) lines. The top ones are for G1, the lower ones, which have much smaller variations with time, are for G2. Finally the red dot-dashed curve and solid dark-green curves near the bottom are for the G2 grid with seventh-order dissipation. The flat curve near the bottom is the horizon mass for Bowen-York data, and dot-dashed curve that runs out of scale near $t = 250M$ is from a BSSN run of these data. Note how much smaller the differences with resolution are for G2. For comparison, the horizon mass for a BSSN evolution and a CCZ4 evolution of Bowen-York data are included. The linear trend in the mass, while convergent, is substantially larger than for Bowen-York.

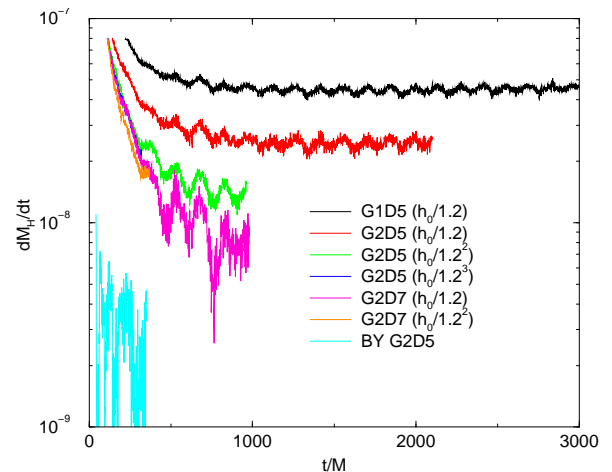


FIG. 8. The rate of horizon mass increase versus time. Here D5 indicated that fifth-order dissipation was used, while D7 indicated that seventh-order was used.

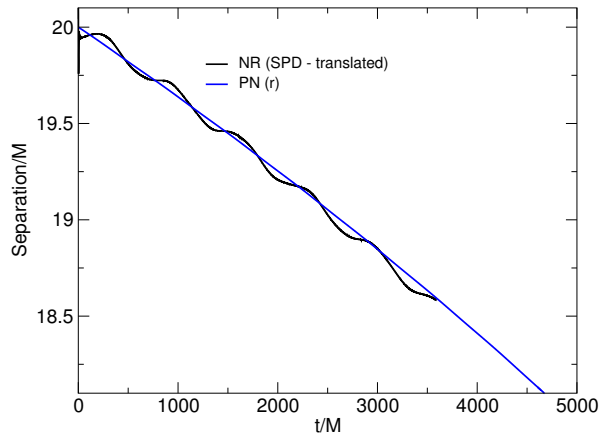


FIG. 9. The SPD and PN separation versus time as calculated using a CCZ4 evolution.

at $r = 1600M$, we get very good agreement between the *raw* ($\ell = 2, m = 2$) mode of ψ_4 and the extrapolation to infinity using the techniques of [46]. Note that the numerical waveform prior to the burst of radiation is purely a function of the initial data. The initial data used the 3.5PN equations of motion, thus the agreement in the frequency at early time with 3.5PN is expected. After the initial data burst, the waveform becomes noisier but the agreement with 3.5PN is still quite good. The numerical waveform amplitude, however, seems to be closer to the average of 1.5 and 3.5PN. All waveforms are shown in Fig. 10.

One important note is that the PN waveform given in the initial data is slightly out of phase with the resulting numerical waveform. This phase error is about 0.255 radians and is apparent at later times in Fig. 11. This will have repercussions if one wants to smoothly attach a PN waveform to the numerical waveform.

The phase error itself can be explained by how we con-

struct the metric in the far zone. In the far zone, the metric at some point at a (coordinate) distance r from the origin depends on the dynamics of the binary at a retarded time given by the light propagation time from the binary to that point. We use the expression $t_{\text{ret}} = t - r$, which is the flat space retarded time. A more accurate expression would include the mass of the spacetime. For a Schwarzschild BH, in harmonic coordinates, the retarded time would be

$$t_{\text{ret}}^{\text{Sch.}} = t - \left[(r + M) + 2M \log \left(\frac{r + M}{2M} - 1 \right) \right], \quad (5)$$

where M is mass of the spacetime. We thus find that for a given waveform frequency ω , using the flat space retarded time will introduce a phase error of approximately

$$\delta\phi = \omega \left[M + 2M \log \left(\frac{r + M}{2M} - 1 \right) \right]. \quad (6)$$

Since the binary's orbital period here is $\Omega_{\text{orb}} \approx 0.01$, and the $(\ell = 2, m = 2)$ mode of the waveform has twice this frequency, we expect a phase error introduced by the flat space retarded time of ≈ 0.287 rad, which is reasonably close to our measured phase error of 0.255 rad.

VI. DISCUSSION

The main questions we addressed here concerned how we can accurately transition from using an analytically (but approximate) evolved spacetime metric—that accurately describes a BHB during the slow inspiral—to a fully nonlinear numerically evolved metric that describes the binary during the rapid plunge and merger. At the transition, we used the analytical spacetime metric to construct initial data for a subsequent numerical evolution. We chose to perform this transition at a binary separation of $D \sim 20M$, where the binary's dynamics are still well described by PN theory.

In order to accurately transition from an analytical evolution to a numerical one, the binary's orbital dynamics could not change significantly as a result of the transition. The binary's dynamics in the fully nonlinear numerical simulation had two main sources of error. First, constraint violations led to rapid unphysical oscillations in the orbital separation. Second, small errors in the PN expressions for the orbital angular momentum and inspiral rate led to eccentricity in the binary. We were able to ameliorate the first source of error by evolving with the constraint-damping CCZ4 formulation of Einstein's equations, which causes constraint violations to rapidly propagated out of the numerical domain, significantly reducing unphysical binary dynamics. In addition, by adding small changes to the initial inspiral rate and orbital frequency, we significantly reduced the eccentricity of the numerical binary.

We subsequently found that the NR evolution leads to both the expected gravitational waveform, orbital frequency, and binary inspiral rate (to within the truncation

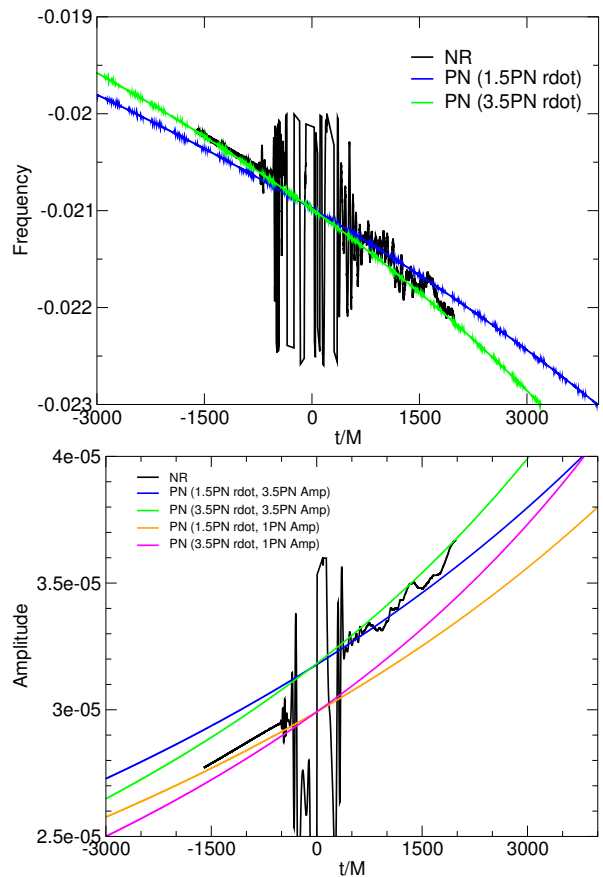


FIG. 10. The frequency and magnitude of the $(\ell = 2, m = 2)$ mode of $r\psi_4$ as measured at $r = 1600M$ in the full numerical simulation and various PN predictions. Here we use either the 1.5PN or 3.5PN expressions for \dot{r} and either the full 3.5PN expression for h_{22} (as a function of r and ω) of Faye et al. [44], or truncate to 1PN order. We use the 3PN expression for ω in all cases.

error of the simulation). The remaining error we found is a phase error in the early part of the waveform. This phase error is about 0.255 rad. We ascribe this error to our use of the flat-space retarded time in the far zone. By not including effects due to the mass of the spacetime we generate phase errors of the order of 0.287 rad in the waveform. This error can itself be ameliorated by using the Schwarzschild retarded time when constructing the far zone metric, which is something we will explore in an upcoming paper.

ACKNOWLEDGMENTS

We thank Carlos Lousto for a careful reading of this manuscript. We thank Carlos Lousto, Zachariah Etienne, and Nicolás Yunes for helpful discussions. The authors are supported by NSF grants AST-1028087, OCI-0725070, OCI-0832606, PHY-0969855, PHY-1125915, PHY-1212426, PHY-1229173, PHY-1305730, Computa-

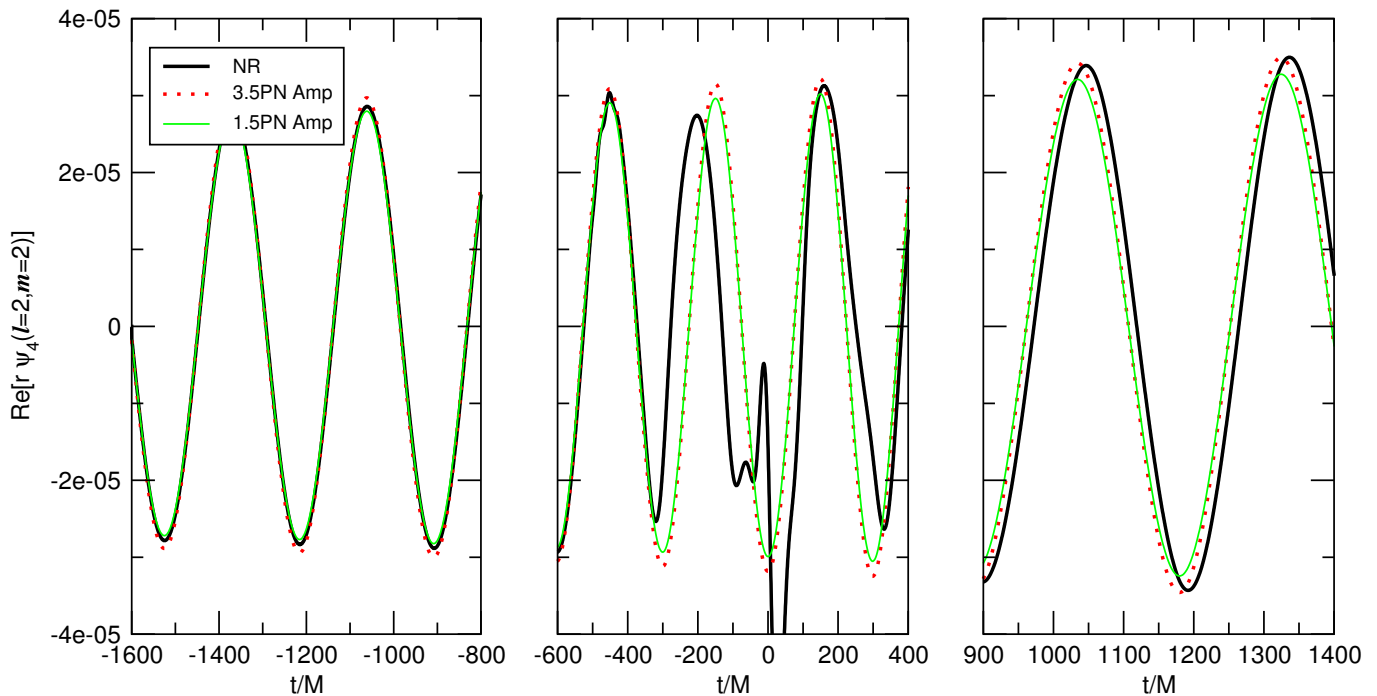


FIG. 11. The numerical and PN waveforms. Here the numerical waveform was time shifted to agree with PN at early times. The phase agreement breaks down after the initial data pulse despite the fact that the late time frequency is still in close agreement with PN. The jump in phase between the early and late part of the waveform is likely due to the use of the flat space retarded time in constructing the early waveform.

tional resources were provided by XSEDE allocation TG-PHY060027N, and by NewHorizons and BlueSky Clusters at Rochester Institute of Technology, which were supported by NSF grant No. PHY-0722703, DMS-0820923, AST-1028087, and PHY-1229173. B. C. M. is supported by the LOEWE-Program in HIC for FAIR.

H. N. acknowledges support by the Grant-in-Aid for Scientific Research No. 24103006. M. Z. is supported by grants 2014-SGR-1474, MEC FPA2010-20807-C02-01, MEC FPA2010-20807-C02-02, CPAN CSD2007-00042 Consolider-Ingenio 2010, and ERC Starting Grant HoloLHC-306605.

-
- [1] F. Pretorius, Phys. Rev. Lett. **95**, 121101 (2005), gr-qc/0507014.
- [2] M. Campanelli, C. O. Lousto, P. Marronetti, and Y. Zlochower, Phys. Rev. Lett. **96**, 111101 (2006), gr-qc/0511048.
- [3] J. G. Baker, J. Centrella, D.-I. Choi, M. Koppitz, and J. van Meter, Phys. Rev. Lett. **96**, 111102 (2006), gr-qc/0511103.
- [4] B. Szilagyi, J. Blackman, A. Buonanno, A. Taracchini, H. P. Pfeiffer, *et al.*, (2015), arXiv:1502.04953 [gr-qc].
- [5] S. C. Noble, B. C. Mundim, H. Nakano, J. H. Krolik, M. Campanelli, Y. Zlochower, and N. Yunes, Astrophys. J. **755**, 51 (2012), arXiv:1204.1073 [astro-ph.HE].
- [6] L. Gallouin, H. Nakano, N. Yunes, and M. Campanelli, Class. Quant. Grav. **29**, 235013 (2012), arXiv:1208.6489 [gr-qc].
- [7] B. C. Mundim, H. Nakano, N. Yunes, M. Campanelli, S. C. Noble, *et al.*, Phys. Rev. **D89**, 084008 (2014), arXiv:1312.6731 [gr-qc].
- [8] M. Zilhao, S. C. Noble, M. Campanelli, and Y. Zlochower, Phys. Rev. **D91**, 024034 (2015), arXiv:1409.4787 [gr-qc].
- [9] M. Zilhao and S. C. Noble, Class. Quant. Grav. **31**, 065013 (2014), arXiv:1309.2960 [gr-qc].
- [10] L. Blanchet, Living Rev. Rel. **17**, 2 (2014), arXiv:1310.1528 [gr-qc].
- [11] N. Yunes, W. Tichy, B. J. Owen, and B. Bruegmann, Phys. Rev. **D74**, 104011 (2006), arXiv:gr-qc/0503011 [gr-qc].
- [12] N. Yunes and W. Tichy, Phys. Rev. **D74**, 064013 (2006), arXiv:gr-qc/0601046 [gr-qc].
- [13] N. K. Johnson-McDaniel, N. Yunes, W. Tichy, and B. J. Owen, Phys. Rev. **D80**, 124039 (2009), arXiv:0907.0891 [gr-qc].
- [14] W. Tichy, B. Brügmann, M. Campanelli, and P. Diener, Phys. Rev. **D67**, 064008 (2003), gr-qc/0207011.
- [15] B. J. Kelly, W. Tichy, M. Campanelli, and B. F. Whiting, Phys. Rev. **D76**, 024008 (2007), arXiv:0704.0628 [gr-qc].
- [16] B. J. Kelly, W. Tichy, Y. Zlochower, M. Campanelli, and B. F. Whiting, Class. Quant. Grav. **27**, 114005 (2010), arXiv:0912.5311 [gr-qc].
- [17] G. Reifenberger and W. Tichy, Phys. Rev. **D86**, 064003 (2012), arXiv:1109.1528 [gr-qc].

- (2012), arXiv:1205.5502 [gr-qc].
- [18] J. M. Bowen and J. York, James W., Phys. Rev. **D21**, 2047 (1980).
- [19] C. O. Lousto and Y. Zlochower, Phys. Rev. **D88**, 024001 (2013), arXiv:1304.3937 [gr-qc].
- [20] C. O. Lousto and J. Healy, (2014), arXiv:1410.3830 [gr-qc].
- [21] Y. Zlochower, J. G. Baker, M. Campanelli, and C. O. Lousto, Phys. Rev. **D72**, 024021 (2005), arXiv:gr-qc/0505055.
- [22] P. Marronetti, W. Tichy, B. Brügmann, J. Gonzalez, and U. Sperhake, Phys. Rev. **D77**, 064010 (2008), arXiv:0709.2160 [gr-qc].
- [23] C. Bona, T. Ledvinka, C. Palenzuela, and M. Zacek, Phys. Rev. **D67**, 104005 (2003), arXiv:gr-qc/0302083.
- [24] S. Bernuzzi and D. Hilditch, Phys. Rev. **D81**, 084003 (2010), arXiv:0912.2920 [gr-qc].
- [25] D. Alic, C. Bona-Casas, C. Bona, L. Rezzolla, and C. Palenzuela, Phys. Rev. **D85**, 064040 (2012), arXiv:1106.2254 [gr-qc].
- [26] H.-O. Kreiss and J. Olinger, Global atmospheric research programme publications series **10** (1973).
- [27] F. Löffler, J. Faber, E. Bentivegna, T. Bode, P. Diener, *et al.*, Class. Quant. Grav. **29**, 115001 (2012), arXiv:1111.3344 [gr-qc].
- [28] P. Msta, B. C. Mundim, J. A. Faber, R. Haas, S. C. Noble, *et al.*, Class. Quant. Grav. **31**, 015005 (2014), arXiv:1304.5544 [gr-qc].
- [29] Einstein Toolkit home page: <http://einstein toolkit.org>.
- [30] Cactus Computational Toolkit home page: <http://cactuscode.org>.
- [31] E. Schnetter, S. H. Hawley, and I. Hawke, Class. Quant. Grav. **21**, 1465 (2004), gr-qc/0310042.
- [32] Fixed Mesh Refinement with Carpet: <http://www.tat.physik.uni-tuebingen.de/~schnette/carpet/>.
- [33] J. Thornburg, Class. Quant. Grav. **21**, 743 (2004), gr-qc/0306056.
- [34] M. Campanelli, B. J. Kelly, and C. O. Lousto, Phys. Rev. **D73**, 064005 (2006), arXiv:gr-qc/0510122.
- [35] S. Brandt and B. Brügmann, Phys. Rev. Lett. **78**, 3606 (1997), gr-qc/9703066.
- [36] Z. B. Etienne, J. A. Faber, Y. T. Liu, S. L. Shapiro, and T. W. Baumgarte, Phys. Rev. **D76**, 101503 (2007), arXiv:0707.2083 [gr-qc].
- [37] J. D. Brown, O. Sarbach, E. Schnetter, M. Tiglio, P. Diener, *et al.*, Phys. Rev. **D76**, 081503 (2007), arXiv:0707.3101 [gr-qc].
- [38] J. D. Brown, P. Diener, O. Sarbach, E. Schnetter, and M. Tiglio, Phys. Rev. **D79**, 044023 (2009), arXiv:0809.3533 [gr-qc].
- [39] C. O. Lousto, H. Nakano, Y. Zlochower, B. C. Mundim, and M. Campanelli, Phys. Rev. **D85**, 124013 (2012), arXiv:1203.3223 [gr-qc].
- [40] T. Nakamura, K. Oohara, and Y. Kojima, Prog. Theor. Phys. Suppl. **90**, 1 (1987).
- [41] M. Shibata and T. Nakamura, Phys. Rev. **D52**, 5428 (1995).
- [42] T. W. Baumgarte and S. L. Shapiro, Phys. Rev. **D59**, 024007 (1999), gr-qc/9810065.
- [43] H. P. Pfeiffer *et al.*, Class. Quant. Grav. **24**, S59 (2007), gr-qc/0702106.
- [44] G. Faye, S. Marsat, L. Blanchet, and B. R. Iyer, Class. Quant. Grav. **29**, 175004 (2012), arXiv:1204.1043 [gr-qc].
- [45] M. Campanelli, C. O. Lousto, H. Nakano, and Y. Zlochower, Phys. Rev. **D79**, 084010 (2009), arXiv:0808.0713 [gr-qc].
- [46] H. Nakano, J. Healy, C. Lousto, and Y. Zlochower, (2015), arXiv:1503.00718 [gr-qc].